Impact of anionic lipids on the energy landscape of conformational transition in anion exchanger 1 (AE1)

Tianle Chen[1,+], Francesca Vallese[2,3,4,5,+], Eva Gil-Iturbe[6], Kookjoo Kim[2,3], Matthias Quick[3,6,7], Oliver Clarke[2,3], and Emad Tajkhorshid[1,*]

[1]Theoretical and Computational Biophysics Group, NIH Resource for Macromolecular Modeling and Visualization, Beckman Institute for Advanced Science and Technology, Department of Biochemistry, and Center for Biophysics and Quantitative Biology, University of Illinois Urbana-Champaign, Urbana, IL, USA

[2]Department of Anesthesiology, Columbia University Irving Medical Center, New York, NY, USA

[3]Department of Physiology and Cellular Biophysics, Columbia University, New York, NY, USA

[4]Structural Biology Initiative, CUNY Advanced Science Research Center, New York, NY 10031, USA

[5]Department of Chemistry and Biochemistry, City College of New York, NY 10031, USA

[6]Department of Psychiatry, Columbia University Irving Medical Center, New York, NY, USA

[7]Area Neuroscience-Molecular Therapeutics, New York State Psychiatric Institute, New York, NY, USA

[*]emad@illinois.edu

[+]these authors contributed equally to this work

September 13, 2024

Abstract

Anion Exchanger 1 (AE1) is an elevator-type membrane transporter that plays a key role in erythrocytes by mediating exchange of chloride and bicarbonate ions across the membrane, thus participating in acid-base homeostasis. While previous studies have provided structural insights into AE1 and its substrate binding, the conformational transitions and role of lipid interactions have remained elusive. In this study, we utilized cryo-electron microscopy (cryo-EM) to resolve three high resolution structure of distinct conformational states of AE1: two inward-facing (IF1 and IF2) and one outward-facing (OF). Furthermore, uptake assay revealed the modulatory effect of phosphatidylinositol 4,5-bisphosphate (PIP_2) lipids on AE1. Molecular dynamics (MD) simulations were conducted on these structures to capture anion binding and determine the anion binding sites in AE1. We then used a combination of advanced enhanced sampling techniques together with system-specific collective variables to study the OF$\Longleftrightarrow$IF transition in AE1 and provide refined pathways for the process in three different systems: *apo*, HCO_3^--bound, and an AE1 system in

which cryo-EM determined interfacial PIP_2 lipids had been removed. These pathways were then used to calculate the free energy of the OF$\Longleftrightarrow$IF transition in AE1 under different conditions. The energies show how substrate binding reduces the energy barrier, and therefore facilitates the transport. Furthermore, they clearly capture the inhibitory effect of PIP_2 lipids at the dimer interface and provide a molecular mechanism for it. These results provide molecular-level understanding of the mechanistic basis for ion transport in AE1 and the regulatory role of PIP_2 on its function.

Introduction

Anion exchanger 1 (AE1), *aka*, band 3, which is encoded by the SLC4A1 gene, is the most abundant membrane protein in human red blood cells (RBCs) accounting for ~25% of their total membrane proteins.[1,2] AE1 facilitates the efficient transfer of carbon dioxide from tissues to the lungs by rapidly transporting the soluble bicarbonate (HCO_3^-) form across the RBC membrane.[3] AE1 mediates electroneutral anion exchange, maintaining charge balance on both sides of the membrane by countertransporting one Cl^- ion against one HCO_3^- during its transport cycle. This results in a gradient-driven, but electroneutral exchange of Cl^- for HCO_3^-, a phenomenon known as the "chloride shift", which enables RBCs to recognize metabolically active tissues and supply them with the required amount of oxygen.[4,5] AE1 mutations have been linked to various diseases including hereditary spherocytosis, Southeast Asia ovalocytosis, and distal renal tubular acidosis.[6-8]

Human AE1 contains 911 residues divided into two domains: an N-terminal, cytosolic domain (CD, residues 1-347) and a C-terminal transmembrane domain (TMD, residues 371 to 911), joined by a flexible linker (residues 348-370). The TMD is responsible for anion transport,[9] while the CD mediates its interaction with ankyrin, protein 4.2, deoxyhemoglobin, and glycolytic enzymes.[10,11] The CD can be removed without affecting AE1 transport function.[12,13] The TMD is composed of 14 transmembrane segments (TMs) which are organized into two inverted repeats with the same fold, TM1-7 and TM8-14.[2] These transmembrane helices are arranged into a core domain, also referred to as the transport domain (TD: TM1-4 and TM8-11), and a gate domain, also known as the scaffold domain (SD: TM5-7 and TM12-14) with the anion translocation pathway located between the two domains. Similar to other facilitated transporters from the SLC4 family, such as the human electrogenic Na^+/HCO_3^- cotransporter 1 (NBCe1) and the fungal borate transporter Bor1, AE1 operates via an elevator mechanism,[14-16] in which the transporter switches between the inward-facing (IF) and outward-facing (OF) states. During this mechanism, the movements of the gate and core domains carry the substrate from one side of the membrane to the other. Recent structural studies have provided insights into substrate-interacting residues and inhibition of AE1, reported for the OF state.[17-19] There is however limited knowledge regarding its IF state,[16] and the mechanism of its transition between the two states is widely unknown.

Lipids are known to play crucial roles in transporters' function by influencing their structure and dynamics. For example, the effect of cholesterol on the ATP-binding cassette super-family G member 2 protein (ABCG2)[20] and PIP_2 (phosphatidylinositol 4,5-bisphosphate) modulated activation of Na^+/H^+ exchangers[21] have been reported. Advances in cryo-EM have expanded the number of lipid-bound membrane protein structures, e.g., AE2 in complex with PIP_2,[22] providing convincing evidence for their roles in transporter regulation. Enrichment and putative binding sites of PIP_2 and cholesterol have been also reported by recent computational studies, e.g., using coarse grained simulations,[23] but their potential functional roles require additional investigations.

In this study, we report the cyro-EM structures of AE1 in both OF and IF states: one OF structure and two IF structures, IF1 and IF2, with different configurations of TM10. Arginine 730 (R730) is observed to be exposed to the lumen in both IF and OF structures, and a large number of Cl^- or HCO_3^- spontaneous binding events in both conformations are captured in 8 independent μs-timescale molecular dynamics (MD) simulations. While there is

consensus on the alternating access mechanism of AE1,[24] the structural transition underlying the process remain uncharacterized. Using driven MD simulation along specific collective variables (CVs) we successfully induced the OF⇌ IF transition and used advanced sampling methods to compute the free energy associated with the process for the apo, substrate-bound, and an AE1 model in which PIP_2 had been removed. The simulations reveal how substrate binding reduces the transition energy barrier and thus facilitates the OF⇌IF conformational change in this antiporter.

As for the role of PIP_2, a binding site for this lipid has been identified at the AE1 dimer interface, and our uptake assay shows an increased transport activity after the depletion of PIP_2. Our computational simulations capture a lower free energy barrier for the transition after depletion of PIP_2 and also explain structurally how the interaction between PIP_2 and the protein could raise free energy barrier when the lipid is present. These findings provide a comprehensive molecular-level understanding of AE1 transport cycle and the regulatory role of PIP_2 lipids in its activity.

Results and Discussion

Cryo-EM structures of AE1

Previously reported structures of AE1 have been solved in the OF conformation[16-18] except for a low-resolution structure of AE1 solubilized in n-dodecyl-β-D-maltoside where the transporter assumes a IF conformation.[16] To stabilize the IF state in native membranes, we incubated human erythrocyte ghost membranes with a membrane permeable lysine-reactive crosslinker (DSP) before membrane solubilization, purification, and reconstitution in lipid nanodiscs. Using single particle cryo-EM, we were able to identify three different conformations for AE1 TMD using 3D classification: two IF states (IF1 and IF2) which are differentiated by the conformation of the TM10 helix that bears the presumed anion-binding residue R730, and the OF state (Fig. 1). AE1 monomers in the IF1 state represent 48%, the OF conformation accounts for 32%, and the IF2 state represents 20% of the total particles. In IF1, the TM10 helix is unwound, with R730 projecting into the inward-facing cleft, while in IF2, TM10 is fully ordered, with R730 interacting with the C-terminal end of the TM3 helix (Fig. 1C). Multiple different configurations of the AE1 dimer were separated by 3D classification, of which three major configurations were refined to high resolution: IF/OF at 2.4 Å, OF/OF at 3.1 Å, and IF1/IF2 configuration at 2.9 Å resolution.

As expected from prior studies,[16-18] AE1 forms a homodimer. TM3 and TM10 are interrupted in the middle of the membrane, creating the appearance of a continuous helix. The three different conformations of AE1 allow us to identify a set of critical residues potentially involved in ion access and binding. The opposite orientations of TM3 and TM10 lead to the formation of a putative, dipole-mediated, anion-binding site,[2] which is alternately accessible to either side of the membrane in the OF and IF states through the elevator movement of the transporter's gate and core domain .[25] The gate domain undergoes the most notable change, particularly in the region that involves TM10. Residue R730, situated within TM10, occupies a crucial position within the putative anion cavity. Recent studies have demonstrated the involvement of this residue in coordinating HCO_3^- within the binding pocket of AE1. In the presence of 100 mM HCO_3^-, a cryo-EM study reported HCO_3^- density near R730.[17] In the OF state, TM10 is well-ordered, with R730 facing the extracellular space. This state was previously analyzed for the human AE1 and shows an organization similar to other SLC4 transporters (e.g., NBCe1 and the sodium-driven chloride/bicarbonate exchanger NDCBE).[14,26] In the predominant IF state, IF1, TM10 is completely unfolded, with R730 accessible to the solvent. We also observed a second IF state, IF2, in which R730 is directed towards the intracellular space but displaced by only 7 Å compared to the OF states.

A comparison of the OF and IF conformations reveals that the transition between the states occurs via rotation of the gate domain around an axis roughly intersecting with the intracellular distal corner (F507). This elevator-like

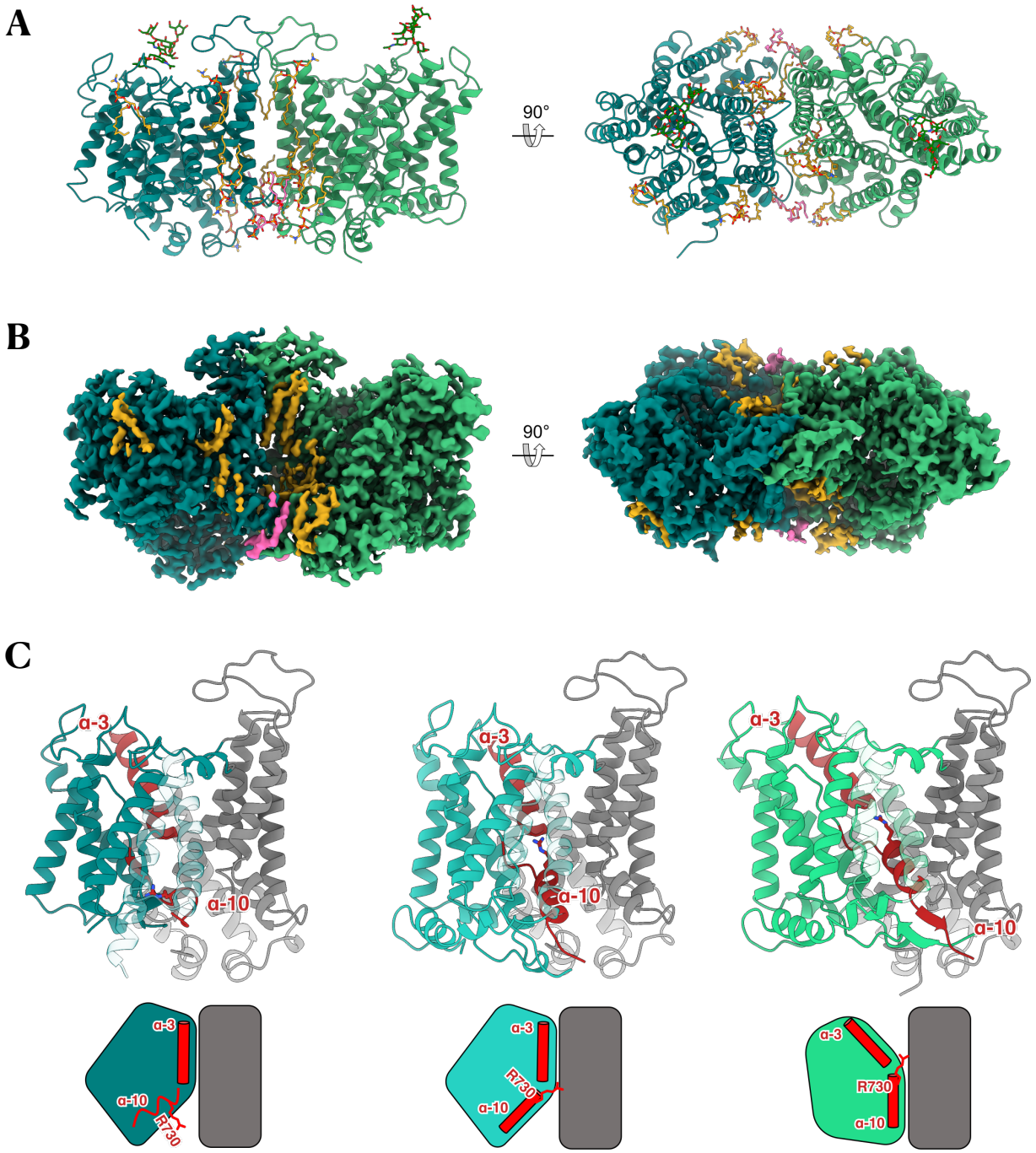

Figure 1: **Three conformations of human AE1 captured by Cryo-EM.** (A) The IF1/OF AE1 dimer viewed from the membrane plane (left) and from the cytoplasm (right). The IF1 and OF conformations are colored in dark and light green, respectively. Lipids are colored in orange, except for PIP_2, which is in pink. (B) The cryo-EM density map of AE1 in IF1/OF configuration. Views and reference colors are the same as in A. (C) AE1 monomer in IF1 (left), IF2 (middle), and OF state (right) along with corresponding schematic representations.

motion is also reported for related transporters, e.g., SLC4A2[22]

PIP_2 at the dimer interface inhibits AE1 activity

Lipid headgroup densities are seen at the intracellular dimer interface on the two sides of the protein, where they bind to patches of positively charged residues 2. Based on the distinctive shape of the densities, we have assigned them as PIP_2[10] (Fig. 2A and B). A series of well-ordered POPC (1-palmitoyl-2-oleoyl-glycero-3-phosphocholine) lipids is also present at the interface between the two protomers, which may contribute to dimer stabilization (Fig. 2C and D). Interfacial lipids have been implicated in maintaining the stability of related dimeric transporters, e.g., in the purine transporter UapA.[27]

PIP_2 plays a critical role in RBC membrane signal transduction.[28] It modulates the interactions between the membrane cytoskeleton and the lipid bilayer, influencing cellular shape and deformability. The identification of this lipid in the AE1 dimeric interface from the cryoEM density between the two protomers (Fig. 2A and B) raises some questions about its possible role in the regulation of AE1. Several amino acids involved in PIP_2 binding are conserved within the SLC4 transporter family, particularly P815 and positively charged residues R602 and K817. R602 is located in the first helical turn of the N-terminal region of TM7, facing back toward the cytosolic loop connecting TM6 and TM7. When mutated to histidine, it causes recessive distal renal tubular acidosis.[29] This suggests that the positive charge at position 602 may be essential for stabilizing the AE1-PIP_2 interaction and, consequently, the dimer interface.

To test whether PIP_2 affects the stability of AE1, we first checked its possible effects on substrate transport using a proteoliposome-based assay. We reconstituted AE1 into liposomes and measured the uptake of $NaHCO_3$ and NaI to assess the transport activity for the two of the established AE1 substrates .[30] To determine AE1's affinity for HCO_3^- and I^- , isotopic dilutions of the radiolabeled anion with increasing concentrations of the unlabeled anion were performed (Supplementary Fig. S1A), yielding an EC50 (effective concentration of the unlabeled anion to reduce the uptake of radiolabeled anion by 50%) of 79 nM for HCO_3^- and 143 nM for I^-. We verified AE1-specific uptake by performing the assays in the presence of DIDS (4,4'-Diisothiocyano-2,2'-stilbenedisulfonicacid), a known anion transporter inhibitor.[31] The uptake levels in the presence of DIDS were reduced by half compared to those without the inhibitor (Supplementary Fig. S1B).

To evaluate the effect of PIP_2 on AE1 function, AE1's uptake activity in proteoliposomes was measured after preincubating it with poly-Lys and phospholipase C (PLC), which cleaves phospholipids just before the phosphate group. Depletion of PIP_2 using PLC, or by using poly-Lys, which shields PIP_2's negative charges, activates AE1-mediated I^- or HCO_3^- uptake (Fig. 2E). Notably, when PIP_2 is removed using PLC before its incorporation into proteoliposomes, an increase in substrate uptake is observed, which is then reversed once new PIP_2 is added (Fig. 2F). These results unequivocally demonstrate the involvement of PIP_2 lipids in regulation of AE1.

Anion binding to AE1 OF and IF states

As an antiporter, AE1 relies on the coupling of downhill electrochemical gradient of one ion to transport another.[32] To gain insight into the binding of anions within the lumen formed between the scaffold domain (SD) and transport domain (TD), we conducted 8 independent 1-μs simulations of membrane-embedded OF/IF2 AE1 in the presence of anions. The system was embedded in a heterogeneous lipid bilayer and solvated with a solution of 18 mM HCO_3^- and 87 mM Cl^-, approximating the average concentrations of these anions in the venous and arterial blood.[33] The hydration map of the lumen (Supplementary Fig. S2A and B) clearly demonstrates that in both the OF and IF states, the central lumen is exclusively exposed to only one side of the membrane (alternating access) from where the anions may diffuse into and out of the protein.

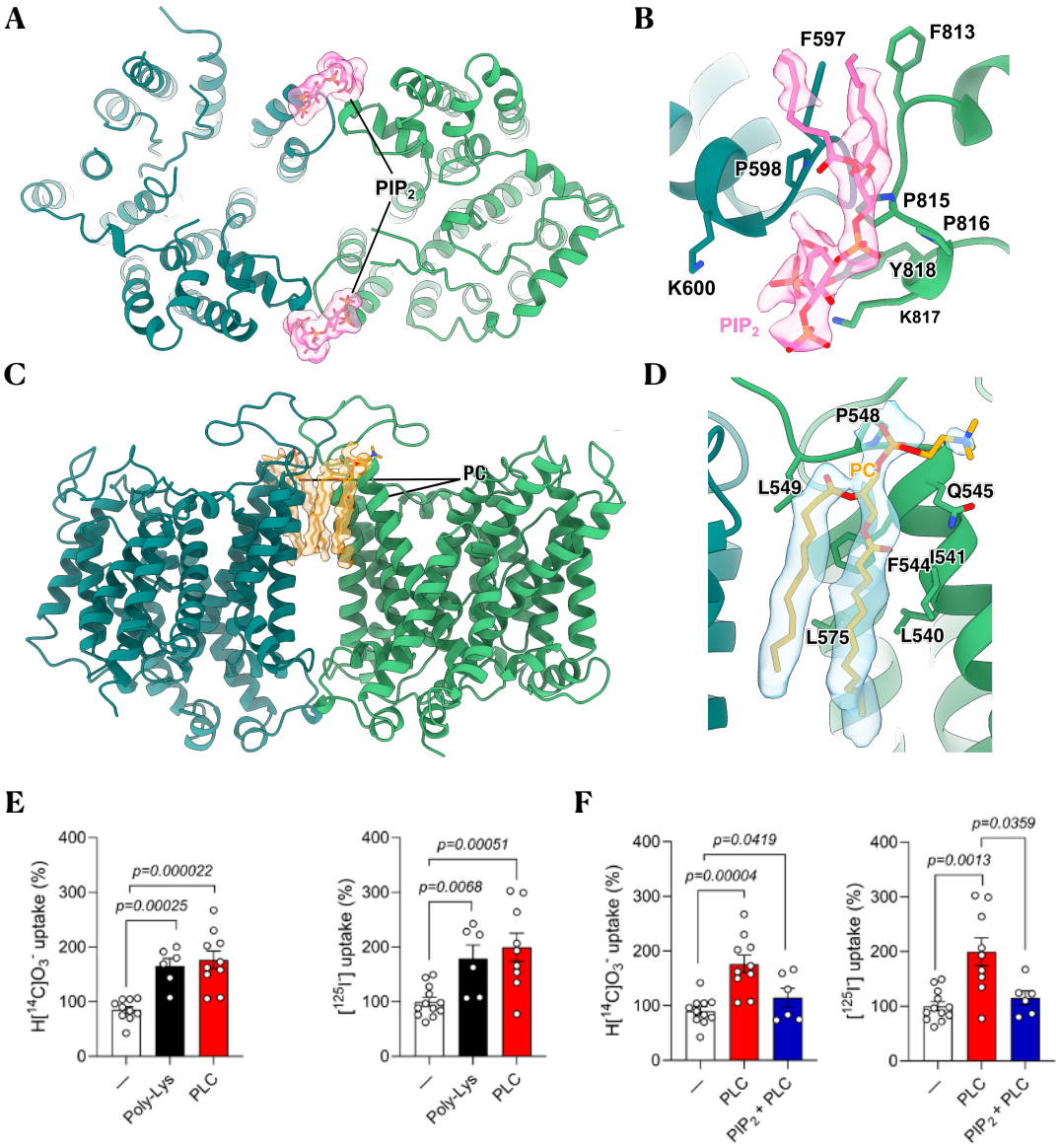

Figure 2: **AE1 in complex with PIP_2 and PC.** (A) Model of AE1 dimer as viewed from inside the cell. AE1 protomers are colored in dark green (IF1 state) and light green (OF state), with PIP_2 molecules in pink. (B) Closeup view of one of the AE1 dimer interfacial PIP_2 lipids. PIP_2 (pink) sit in the middle of the interface. The key residues that interact with the lipid are shown in a stick representation. (C) Model of AE1 dimer as viewed in the plane of the membrane. AE1 protomers are colored in dark green (IF state) and light green (OF state), and molecules of PC are shown in orange. (D) Closeup of the interactions between AE1 protomers and a PC lipid (orange). The key residues that mediate lipid interactions are shown in stick representation. (E-F). 1-min uptake of 10 µM $NaH[^{14}C]O_3$ or $Na[^{125}I]$ by AE1-containing proteoliposomes. AE1 was incubated for 1 h with 15 mg/mL poly-lysine (Poly-Lys), 0.3 U/mL PLC before being incorporated into proteoliposomes. In (D), 50 µM PIP_2 was added to liposomes previously treated with PLC.

Over the collective course of 8 µs sampling, recurring occurrences of Cl^- or HCO_3^- binding to and unbinding from the protein lumen were observed for both OF and IF conformations. One such HCO_3^- binding event is highlighted in Supplementary Movie 1. Averaged over the simulations, the spatial distribution of these anions in the vicinity of AE1 is shown as a volumetric map in Fig. 3A and B, along with their probability density projected over the membrane normal (z-axis) (Supplementary Fig. S2C). The luminal anion distributions within the OF and IF states are distinct, with the probabilities exhibiting two different peaks around $z = -5$ and $z = 5$ Å, respectively. These regions in the OF and IF states are both accessible to R730. A high-density anion site is also observed near the cytoplasmic opening in both OF and IF states (localized at $-15 \leq z \leq -10$ Å) where multiple positive residues from TM6 and TM7 are located, including K590, K592, K600, R602, and R603. These residues clearly play a role in attracting and recruiting free anions from the solution.

To further characterize the anion binding sites in AE1, we ranked the luminal residues interacting with anions during the simulations. The analysis revealed that, in the OF state, R730 consistently forms direct contacts with the anions (Fig. 3C). Additionally, we found that E535 coordinates with the bound bicarbonate through a hydrogen bond with the anion's hydroxyl group in (~70%) of anion binding events. In the IF state, R730 and R589 are the top anion-binding residues, both with a probability of ~50% for directly contacting bound anions (Fig. 3D). R589 is positioned deep in the lumen and close to R730, forming together a highly positively charged site, and the anions can move between them upon entering.

These findings are largely consistent with recent computational and cryo-EM studies.[16,17] The simulations clearly depict binding events where HCO_3^- and Cl^- ions enter and remain within the lumen, establishing stable interactions with the key residue, R730. We further identified other luminal residues that contribute to anion binding, enhancing our understanding of the binding sites and mechanism in AE1.

Next, in order to derive information about the kinetics of anion binding, we approximated the binding affinities for Cl^- and HCO_3^- based on the time courses of anion interactions with residues (Fig. 3E, F, G and H). Our calculations yield estimates for dissociation constant K_d values of 255 mM for Cl^- and 22 mM for HCO_3^- in the OF state. For the IF state, the K_d values are estimated to be somewhat larger, 364 mM for Cl^- and 38 mM for HCO_3^-. These values appear to be relatively high, e.g., compared to an NMR estimate of 5.4 mM for HCO_3^-.[34]

Constructing the OF⟺IF transition pathway

Central to the transport reaction catalyzed by antiporters like AE1, the binding of the substrate to the transporter is essential to initiate the conformational changes that bring about the alternating access mechanism.[35,36] To characterize the underlying structural basis for the alternating access mechanism and how PIP_2 lipids might influence the state transition, we employed enhanced sampling techniques to reconstruct the transition in three systems: substrate-free (*apo*) AE1, a substrate-bound state (with HCO_3^-) identified during our spontaneous ion-binding simulations, and a HCO_3^--bound model in which the cryo-EM resolved PIP_2 lipids at the interface were removed. Conformational transition was realized using driven simulations employing two CVs[37] designed based on our previous experience with elevator transporters,[38,39] z and θ, which represent the distance between the centers of masses of the TD and SD helices and their relative orientation, respectively (Fig. 4A). These CVs cover the translation and reorientation of the TD with respect to the SD, which are the major structural differences between the OF and IF states.

Additionally, we explored three protocols of the two CVs to optimize the biasing protocol: inducing rotation first and translation next, applying them in the reverse order, or simultaneously driving both CVs[40] (Supplementary Fig. S3A). The non-equilibrium works accumulated during these exploratory simulations indicate that the most efficient approach is simultaneously driving the two CVs (Supplementary Fig. S3B). In all three systems, the same protocol was applied when inducing state transition. The Cα RMSD of the helices with respect to the target IF state

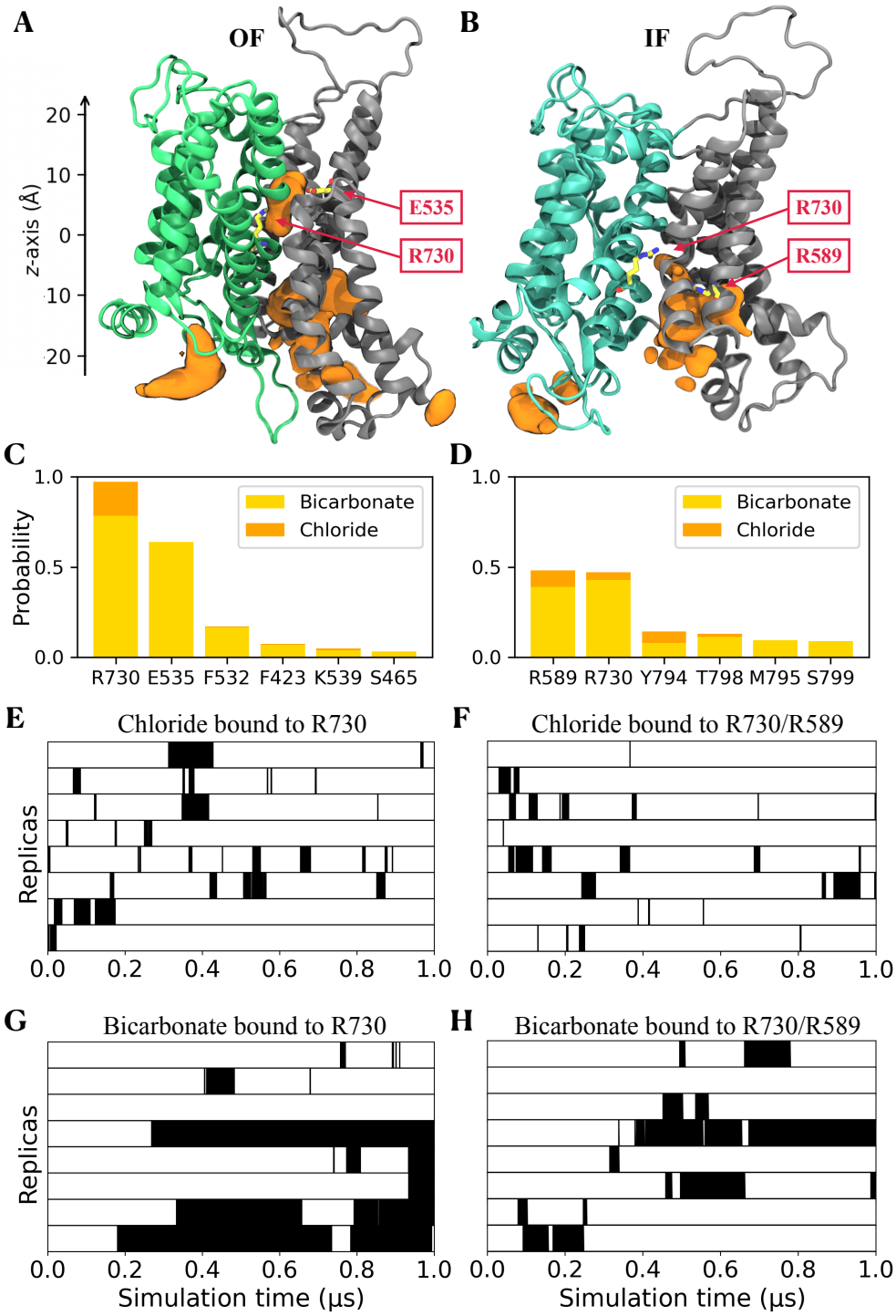

Figure 3: **Spontaneous anion binding to AE1 captured in MD simulations.** (A and B) The anion spatial distribution in the OF (A) and IF (B) states. The TD is shown in green and the SD in grey. The regions for anion binding are shown as orange volumetric surfaces. The main anion-interacting residues are shown in licorice and labeled. (C and D) Probability of major luminal residue to interact with anions among all binding events in the OF (C) and IF (D) states. For each residue in the diagram, interactions with Cl^- are represented in orange, and interactions with HCO_3^- are shown in yellow. (E and F) Cl^- interactions in the OF (E) and IF (F) states during the simulations. The black regions represent the time intervals during which anion binding events occurred. (G and H) HCO_3^- interactions in the OF (G) and IF (H) states during the simulations.

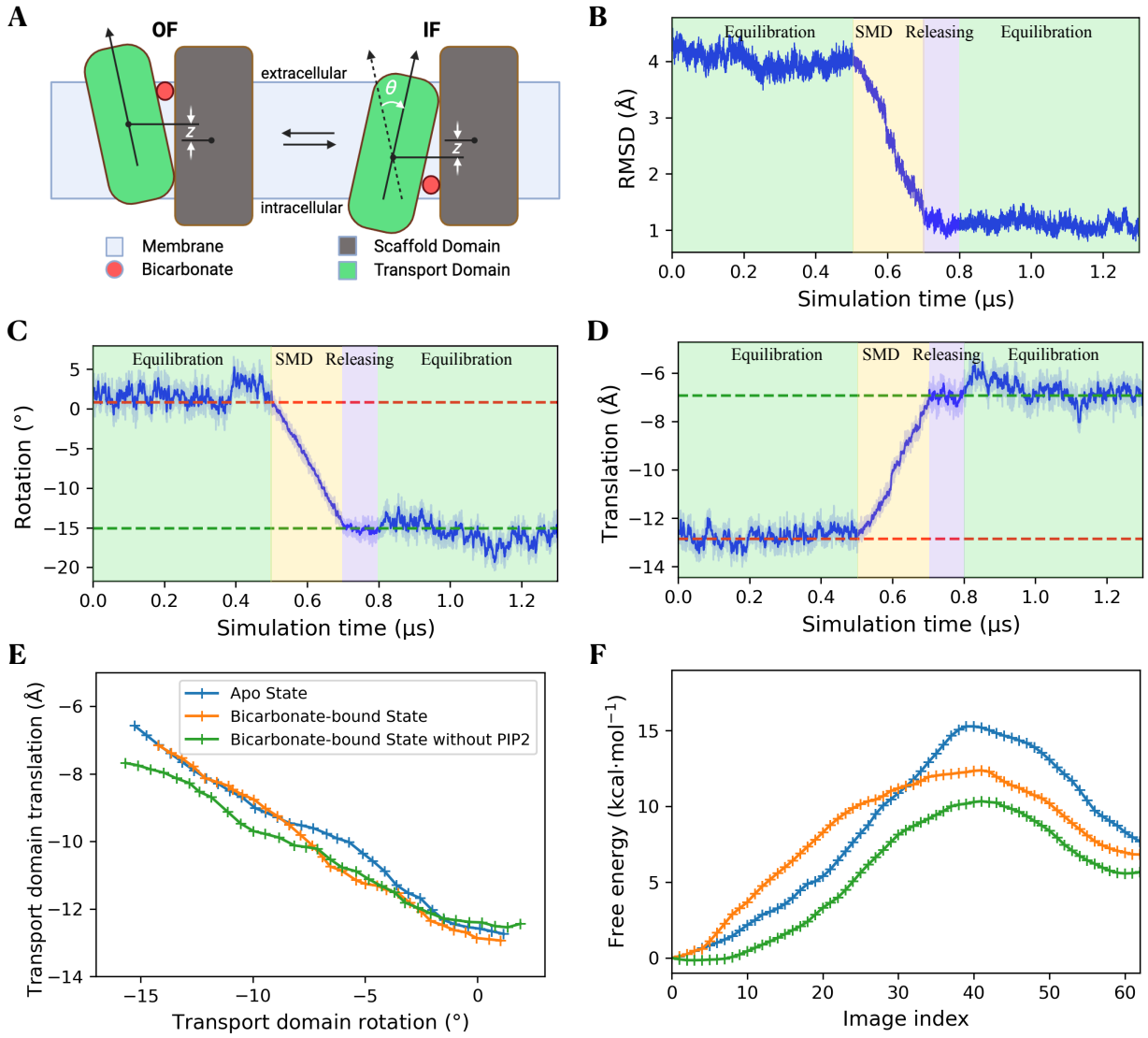

Figure 4: **Conformational transition between the OF and IF states.** (A) Schematic of the elevator mechanism of the OF ⇔ IF transition. The definition of the two CVs is shown, where z and θ denote the translational and rotational motions of the TD relative to the SD, respectively. (B) C_α RMSD of the TM helices during the driven simulations with respect to the target structure in the IF state. (C and D) The change of the CVs for the rotation (C) and translation (D) during the equilibration, driven, releasing, and free simulations, highlighted with different background colors. The CV values of initial and target structures are shown as the dashed red and green lines, respectively. (E) The transition pathways refined using SMwST for *apo* (blue), substrate-bound (orange), and PIP_2-removed (green) systems. The points represent the averaged centers of 8 replicas for 32 "swarms". (F) Free energy profiles computed using BEUS with 64 windows for *apo*, substrate-bound, and PIP_2-removed systems. Same colors as in Panel E.

decreases from 4 to approximately 1 Å and remains stable throughout the post-pulling, free equilibration stage (Fig. 4B and Supplementary Fig. S4A and B). The CV values also reach their target values and remain there even after the restraints are fully released, indicating that the protein has successfully transitioned into a stable IF state (Fig. 4C and D and Supplementary Fig. S4).

Once the system reaches a stable IF conformation, restraints used to maintain the substrate in the binding pocket during the transition are removed, and it is observed that HCO_3^- spontaneously diffuses out of the protein lumen into the cytoplasm during the final equilibration stage, thereby completing its transport across the membrane (Supplementary Fig. S5B and C). The induced conformational changes and the substrate transport are demonstrated in Supplementary Movie 1. This observation is yet another indication that the cytoplasmic gate had entirely opened (alternating access) in the final IF state, allowing the substrate to be released into the solution.

Since the initial estimate of the transition pathway is obtained from driven simulations, it is necessary to relax it into a more accurate description of the pathway. The string method with swarms of trajectories (SMwST; see Methods) was utilized for the refinement of the initial transition pathway.[41] After 200 iterations of SMwST simulations for multiple replicas, involving a cumulative 3 µs of sampling for each system, the strings in the CV space drift from the original trajectory and eventually converge (Fig. 4E and Supplementary Fig. S6A, B and C).

To gain insights into the thermodynamics of the transport and how substrate binding might impact the free energy of the conformational changes during the transport cycle, the refined transition pathways are used to calculate the free energy profiles using bias-exchange umbrella sampling (BEUS) simulations.[42] The free energy profiles for the OF⇌IF transition (Fig. 4F) obtained from reweighting the sampling features an energy barrier separating the OF and IF states. Notably, the IF state occupies a higher free energy basin compared to the OF state. The elevated free energy of the IF state could explain its lower prevalence in our and previous structural studies .[17-19]

Effect of substrate binding on the free energy profile

Comparing the free energy landscapes of the substrate-bound and *apo* forms shows a clear preference for conformational changes when the substrate is bound, as indicated by a lower free energy barrier by approximately 3 kcal/mol (Fig. 4F). This explains why substrate binding is crucial for the global transition in AE1 as an antiporter.

To further explore the structural changes occurring during the OF⇌IF transition and the effect of substrate binding, specific residue-residue interactions near R730 and at the domain interface are analyzed. The region around R730 displays distinct intermediate conformations during the transition in the *apo* and substrate-bound systems in Fig. 5. For example, the space formed by the following two distances can demonstrate the mechanistic difference due to substrate binding: the distances between the R730 guanidinium group and the F532 aromatic ring and to the F464 backbone oxygen. These distances are monitored along the refined pathways and averaged over multiple replicas for each point on the string (Fig. 5).

In both end states (OF and IF states), R730 is relatively free and flexible and does not engage in any stable interactions, resulting in significant fluctuations of all residue-residue distances involving this residue. In the *apo* transition state, R730 forms a hydrogen bond with the backbone of F464 (Fig. 5B). They stay mostly within 2.6-3.0 Å, and thus R730 is kept far from F532 in the SD. During the transition in the substrate-bound protein, and as the TD moves towards the intracellular side, the HCO_3^- is translocated deeper into the central lumen and comes in contact with the hydroxyl group of S465, establishing a hydrogen bond (Fig. 5D). The steric effect of the substrate alters the conformation of R730 causing it to establish a contact with F532 in the SD, which we believe is responsible for stabilizing the transition state and lowering the energy barrier of the transition.

Such cation-π interactions have been shown to be responsible for stabilizing both the overall protein structure and specific conformational states.[43-45] This observation is in line with the previous mutagenesis study where mutating

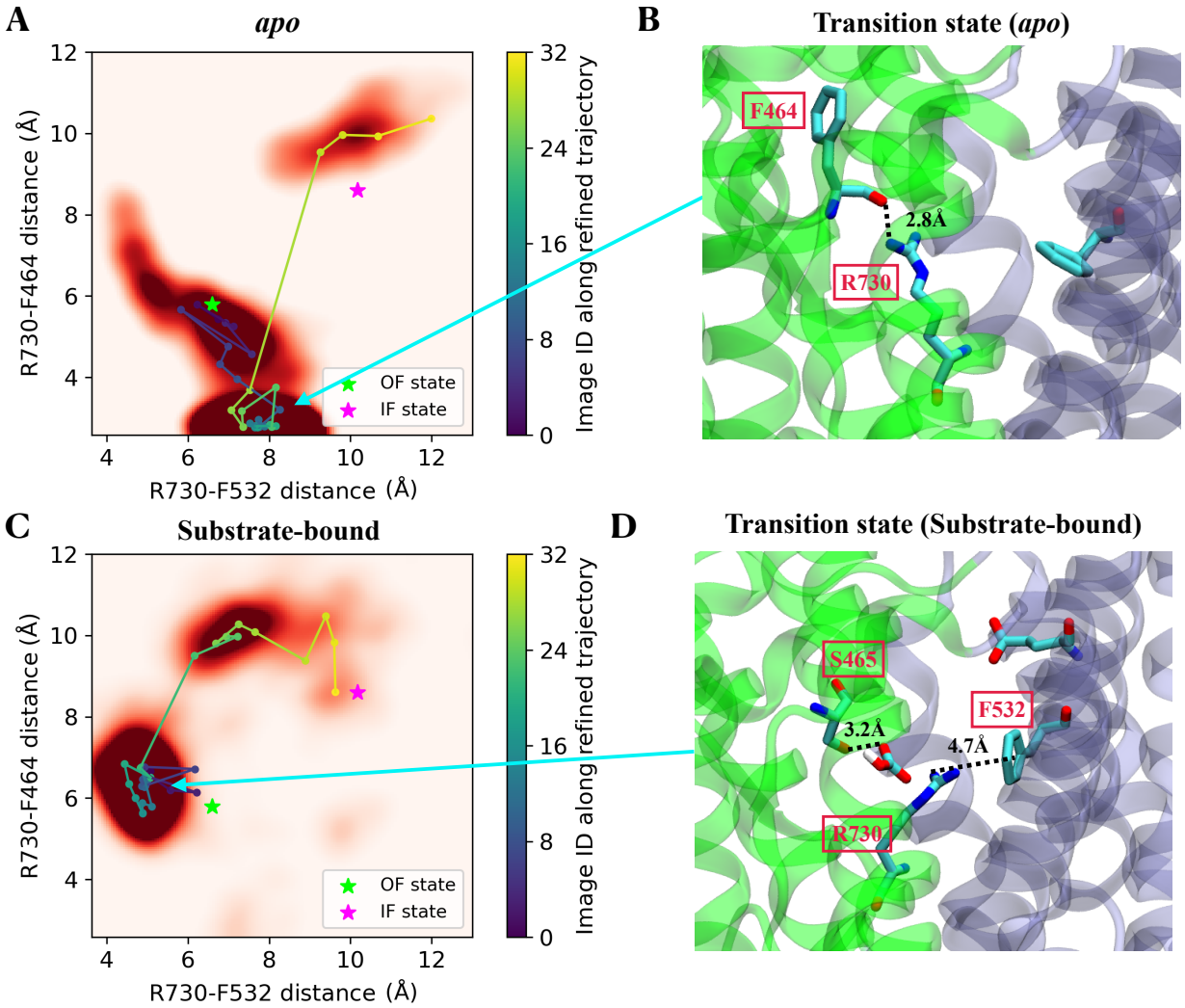

Figure 5: **Effect of substrate binding on the mechanism of transition.** (A) Distribution of R730-F532 and R730-F464 distances during SMwST simulations for the *apo* system. The darkness of the red color indicates the density of sampling, with darker regions corresponding to higher sampling densities. Stars denote the locations of the OF and IF states, averaged from equilibrium simulations. Colored data points (represent average values per window (0 to 31 in SMwST; scale bar), with connecting lines indicating the refined transition pathway from OF to IF. (B) Molecular view of the transition state in the *apo* system, where the R730 interacts with the F464 backbone. (C) Distribution of R730-F532 and R730-F464 distances in the substrate-bound system. (D) Molecular view of the transition state in the substrate-bound system, highlighting R730's contact with F532 due to the hydrogen bond formed between HCO_3^- and S465.

S465 significantly reduced the activity but mutation of F464 had no effect.[46]

Impact of PIP_2 interaction on the transition

Comparing the transitions in the substrate-bound and PIP_2-removed systems provides molecular details for how PIP_2 might influence AE1 activity. Firstly, during equilibrium simulations, among all the lipids resolved by cryo-EM (Fig. 1A and B), the interfacial PIP_2s located near the dimer interface exhibit the highest stability as indicated by their small RMSD and fluctuation (Supplementary Fig. S7). Interactions of the PIP_2 headgroup with K600, R602, and R603 in the SD appear to be important elements for stabilizing the lipid binding pose. Although the PIP_2 lipids are situated between the two SDs, a notable difference between the OF and IF states is the interaction of one of them with an intracellular β-hairpin-containing loop from the TD between TM10 and TM11 as shown in Fig. 6A and C. K743 in this hairpin forms a salt bridge with the 4- or 5-phosphate groups in the PIP_2 headgroup, resulting in its stability throughout the 1 µs simulation time (Fig. 6B and E). This contact needs to break before reaching the IF state, in which K743 and the lipid are separated by 20-30 Å (Fig. 6D and E). Notably, the loop and PIP_2 are far from each other in both IF1 and IF2 states. Similar interactions between PIP_2 and the β-hairpin were also highlighted in previous coarse-grained simulations.[23]

As expected, a sudden dissociation of this salt bridge is observed during the driven simulations of the transition from the OF to the IF state (Fig. 6F and Supplementary Movie 1). Note that only the TM helices are biased in driven simulations, and the β-hairpin loop is free of any restraints/biases during this phase. As calculated using BEUS, the free energy barrier for the OF to IF transition in the PIP_2-removed system is approximately 2 kcal/mol lower than that of the native state (Fig. 4F), indicating an increased rate of conformational change. This finding aligns with our experimental results, which show that the removal of PIP_2 increases AE1's functionality. A previous study on bicarbonate transporter-related protein-1 (BTR1) also demonstrated that disruption of the PIP_2 binding site can shift the transporter into an IF conformation.[47] These results explain our experimentally measured inhibitory effect of PIP_2 on AE1 activity, highlighting the potential functional role the TM10-TM11 loop in the transporter's function.

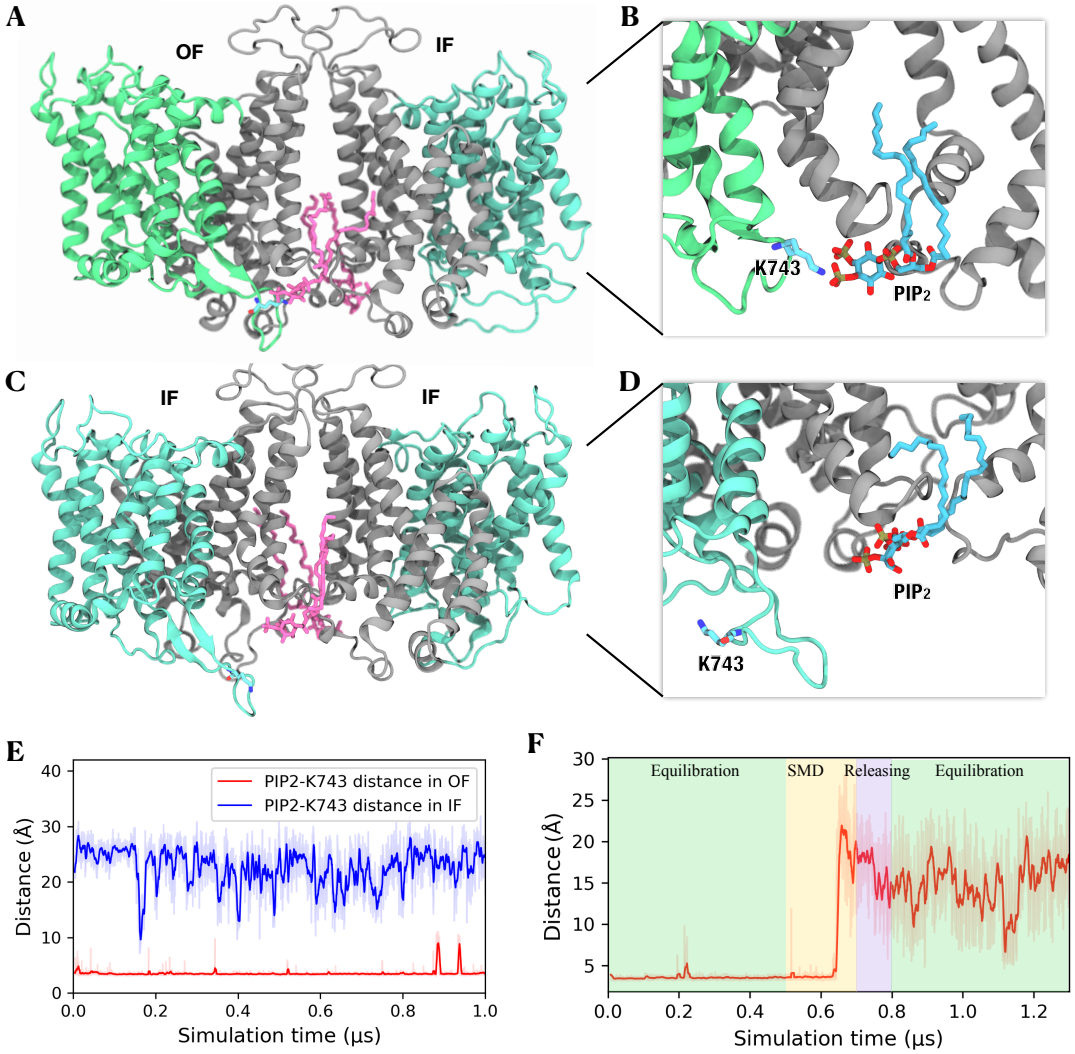

Figure 6: **Mechanism of PIP_2 effect on the conformational transition.** (A) Molecular view of the PIP_2-β-hairpin interaction in the OF state, with PIP_2 in pink and K743 of the loop in licorice. (B) Minimum distance between heavy atoms of PIP_2 and K743 for OF (red) and IF (blue) states. (C) Molecular view of the system after the protein has reached the IF state. (D) PIP_2-K743 distance during the SMD simulations of transition from OF to IF.

Concluding Remarks

Membrane transporters often undergo large conformational changes to accomplish their function. Capturing these changes, which take place within the viscous environment of a membrane and are usually slow for timescales accessible to molecular simulations, is challenging. The current study presents a joint experimental and computational study investigating various structural and functional aspects of an antiporter, AE1, one of the highest abundance membrane proteins in the RBCs, which is responsible for the exchange of Cl^- and HCO_3^- across the membrane. Using cryo-EM measurements we have solved the structures of the transporter in both IF and OF states within a membrane environment at high resolutions. The OF/IF dimeric structure was then used in a sizeable set of μs MD simulations, which captured spontaneous binding events of Cl^- or HCO_3^- to AE1's lumen indicating the key role of R730 for substrate binding in both states and for the transport process. Using advanced enhanced sampling techniques, we then simulated the transition between the two states under different conditions, namely, in *apo* and substrate-bound AE1, and in a system where dimeric PIP_2 lipids had been removed. Refined transition pathways from these simulations were used to calculate the free energy of the transition in these systems. The results not only substantiate how substrate binding is needed for the transition in this antiporter, they also show how PIP_2 binding at the dimeric interface increases the energy barrier against the transition and therefore slows it down, an effect that we had also measured experimentally in our uptake assays. As such, the study provides yet another example of a membrane protein whose function is modulated by signaling lipids.

Methods

AE1 sample preparation for cryo-EM

Erythrocyte ghost membranes were prepared as described by Niggli et al. 2016.[48] Ghost membranes (~3 g) were incubated with 2.5 mM DSP (dithiobis(succinimidyl propionate)) crosslinker in 10 mM Hepes (pH 7.4), 130 mM KCl at room temperature for 30 min. The cross-linking reaction was quenched by the addition of 20 mM Tris-HCl, pH 8. Membranes were washed 3 times with low-salt buffer (10 mM HEPES, 0.1 M KCl, 0.5 mM dithiothreitol (DTT), 0.5% Triton X-100, and 1 mM EDTA, pH 7.4), followed by incubation in high salt buffer (10 mM Hepes, 1 M KCl, 0.5 mM DTT, and 0.5% Triton X-100, pH 7.5 and protease inhibitors) on ice for 30 min. Unsolublized material was pelleted by centrifugation (100k × g, 30 min), and the supernatant containing solubilized proteins were concentrated using a 100 kDa centrifugal concentrator (Millipore). The sample was then loaded on a glycerol gradient (12-28% glycerol in HEPES 10 mM, NaCl 130 mM and 0.05% Triton X-100, pH 7.5), and centrifuged for 15 h at 25,000 rpm (Beckman SW 32 rotor). The fractions enriched with AE1 protein were collected and incorporated into lipid nanodiscs with a 1:5:250 molar ratio of protein, membrane scaffold protein (MSP-1E3D1) and POPC (Avanti polar lipids). The protein in MSP nanodisc was then subjected to a first gel filtration run using a Superdex 200 10/300 Increase column (Cytiva) and the main peak, close to the void volume of the column, was collected and then further purified using a Superose 6 increase 10-300 column (Cytiva) (Supplementary Fig. S8). 3 µL of purified AE1 at 5 mg/mL was added to a glow discharged (PELCO easiGlow) 0.6/1 µm holey gold grid (Quantifoil UltrAuFoil) and blotted for 4-6 s at 4°C and 100% humidity using the Vitrobot Mark IV system (Thermofisher Scientific), before plunging immediately into liquid ethane for vitrification. Cryo-EM data were collected on a Titan Krios electron microscope (Thermofisher Scientific) equipped with a K3 direct electron detector (Gatan) operating at 0.83 Å per pixel in counting mode using Leginon automated data collection software .[49] Data collection was performed using a dose of 58 e^-/Å^2 across 50 frames (50 ms per frame) at a dose rate of 16 e^-/pixel/s, using a set defocus range of −0.5 to −1.5 µm. A 100-µm objective aperture was used. A total of 20,464 micrographs were collected.

Cryo-EM data processing

The final cryo-EM data processing workflow is summarized in Supplementary Fig. S9. Orientation distributions, FSC plots, and validation statistics are presented in Supplementary Figs. S10, S11, S12, and Table S1. Maps and raw movies have been deposited at EMDB (IDs: xxx) and EMPIAR (IDs: yyy). Patch-based motion correction and dose-weighting of 20k movies was carried out in cryoSPARC using the Patch Motion job type. Subsequent steps were performed in cryoSPARC v3.2 and v3.3 unless otherwise indicated.[50] Patch-based CTF estimation was performed on the aligned, non-dose-weighted averages using Patch CTF. Particle picking was performed using crYOLO,[51] and then coordinates were imported into cryoSPARC. The initial set of 4,942,577 particles were imported for extraction, ab-initio reconstruction, and heterogeneous refinement which resulted in 1,390,266 particles. Subsequent non-uniform refinement of the selected particles resulted a map at 3.02 Å. Three rounds of Bayesian polishing of this set of particles were executed in RELION 4.[52] Between each two rounds of polishing, we imported the polished particles into cryoSPARC, followed by non-uniform refinement including on-the-fly per particle defocus refinement and refinement of higher order CTF parameters (beam tilt and trefoil). The final round of polishing gave a 2.45 Å resolution reconstruction, with significantly improved density quality.

The polished particles were subjected to heterogeneous refinement using four AE1 classes as inputs, as well as three decoy classes, using a batch size per class of 10,000 particles. After heterogeneous refinement, the particles in the four AE1 classes (1,286,208 particles) were combined and used for 3D classification without alignments. 3D classification without alignments, requesting 50 classes, allowed the identification of 3 conformations for the AE1 monomer, corresponding to the IF1, IF2 and OF states. Combining different classes containing these conformations gave three maps – the IF1-OF state at 2.4-Å resolution (666k particles), the OF-OF state at 3.11-Å resolution (109k particles), and IF1-IF2 state at 2.88-Å resolution (79k particles). Atomic models of AE1 in the three different conformations were built in Coot[53,54] using AE1 in the OF state (PDB:4YZF) as a starting model, followed by refinement using phenix.real_space_refine (PMID: 29872004). Model and density visualizations were prepared using ChimeraX.[55]

Mass Photometry (MP, iSCAMS)

Mass photometry experiments were performed with a Refeyn OneMP (Refeyn Ltd.). Data acquisition was performed using AcquireMP (Refeyn Ltd. 172 v2.3). Samples were evaluated with microscope coverslips (cover glass thickness $1.5 \times 24 \times 50$ mm, Corning). The coverslips were washed with ddH_2O and isopropanol. A silicone template was placed on top of the coverslip to form reaction chambers immediately prior to measurement. The instrument was calibrated using NativeMark Protein Standard (Thermo Fisher). 10 µL of fresh room-temperature buffer was pipetted into a well, the focal position was identified and locked. For each acquisition 1 µL of the protein (at a concentration of 200 nM) was added to the well and thoroughly mixed. MP signals were recorded for 60 s to allow detection of at least 2×10^3 individual protein molecules. The data were analyzed using the DiscoverMP software.

Proteoliposomes preparation

Purified AE1 was reconstituted into preformed liposomes composed of POPC at a protein-to-lipid ratio of 1:150 (w/w) following a previously described protocol.[56] The lumen of the proteoliposomes was composed of 50 mM KPi, pH 7.5 and 10 mM $NaSO_4$ to promote the exchange with the substrates. To maintain their stability, the proteoliposomes were aliquoted, rapidly frozen in liquid nitrogen, and stored at −80°C. In all experimental setups, liposomes with the same composition but lacking the AE1 protein were used as a control.

Liposome-based, radiolabeled uptake assays

Uptake of 10 μM Na[^{125}I] (0.5 mCi/mmol) and NaH[^{14}C]O_3 (58 mCi/mmol, both American Radiolabeled Chemicals, Inc.) was performed in AE1-containing proteoliposomes (~50 ng AE1 per transport assay) in 50 μL assay buffer composed of 110 mM KPi, pH 7.5, 10 mM $NaSO_4$ over 10-second periods in the presence or absence of compounds as indicated in the figure legends. The reactions were quenched by the addition of ice-cold 100 mM KPi, pH 6.6 and 100 mM LiCl and filtered through 0.45 μm nitrocellulose filters (Millipore). Dried filters were incubated in scintillation cocktail, and the retained radioactivity on the filters was determined by scintillation counting (Hidex, SL300). The specific uptake activity of AE1 was determined by subtracting the background signal determined in control liposomes (lacking AE1) from the signal measured in AE1-containing proteoliposomes and normalized to the specific signal in the absence of compound. AE1 was incubated for 1 h with 15 mg/mL poly-lysine (Millipore Sigma), 0.3 U/mL PLC (Invitrogen) before being incorporated into proteoliposomes. 50 μM PIP_2 (Millipore Sigma) was added to the protoliposomes, and incubated for 1 h, after protein incorporation into the proteoliposomes. Then the uptake of 10 μM NaH[^{14}C]O_3 or Na[^{125}I] by AE1-containing proteoliposomes was measured for 1 min. Statistical analysis of the data was performed in GraphPad Prism 10 as appropriate. Data are mean ± s.e.m. of n = 3. P values were obtained with a two-tailed Mann-Whitney test.

Simulation system preparation

For MD simulations, we used the IF2/OF AE1 dimer structure taken from the cryo-EM data. The cryo-EM structure lacked coordinates for specific loops, which were constructed using the Rosetta *ab-initio* fragment assembly within the Robetta protein structure prediction server.[57] The protonation states of the titratable residues were determined with PROPKA.[58] From the cryo-EM density map, several lipids, including PIP_2 and POPC, were discernible, either at the dimer interface or elsewhere near the protein. Only the coordinates for the lipid head groups and first few carbons of their tails could be assigned based on the density map. The complete lipid tails were then reconstructed using PSFGEN plugin in VMD[59] according to their topology. To represent the cellular environment, we generated a heterogeneous lipid bilayer using the CHARMM-GUI's Membrane Builder tool,[60,61] designed to replicate the lipid composition in human RBCs with a total of 210 lipids (cholesterol: PC: PE: SM: PS: PIP_2: PIP_3 = 45: 16: 15: 14: 8: 1: 1).[62,63] The PPM (Positioning of Proteins in Membrane) Server was used to determine the initial orientation and insertion depth of AE1 in the membrane.[64] Upon combining the membrane and protein, the experimentally resolved PCs and PIP_2s were preserved, and we removed all other lipids placed by CHARMM-GUI positioned within 1 Å of the protein or resolved lipids. Subsequently, the membrane-embedded protein system was solvated with a solution including 1.8 mM HCO_3^- and 87 mM Cl^- using the VMD Autoionize plugin. Sodium ions were added for charge neutralization. The assembled system spanned dimensions of approximately 145×145×125 $Å^3$, containing 276k atoms. Lastly, to introduce variability in the lipid environment surrounding the protein in different simulation replicas, we generated multiple copis by shuffling all the lipids (excluding the cryo-EM bound ones) within the same leaflet, employing the VMD Membrane Mixer plugin.[65] (Fig. 7)

Equilibrium simulations

MD simulations were performed using a highly scalable MD engine, NAMD3,[66,67] using the CHARMM36 and CHARMM36m forcefields.[68,69] Simulations were conducted under the NPT ensemble, maintaining the temperature at 310 K with the Langevin thermostat.[70] The Nosé–Hoover Langevin piston method was used to hold the pressure at 1 bar.[71,72] Non-bonded interactions were computed with a 12-Å cutoff and a switching distance of 10 Å. Long-range electrostatic interactions were computed using the particle mesh Ewald method under periodic boundary condi-

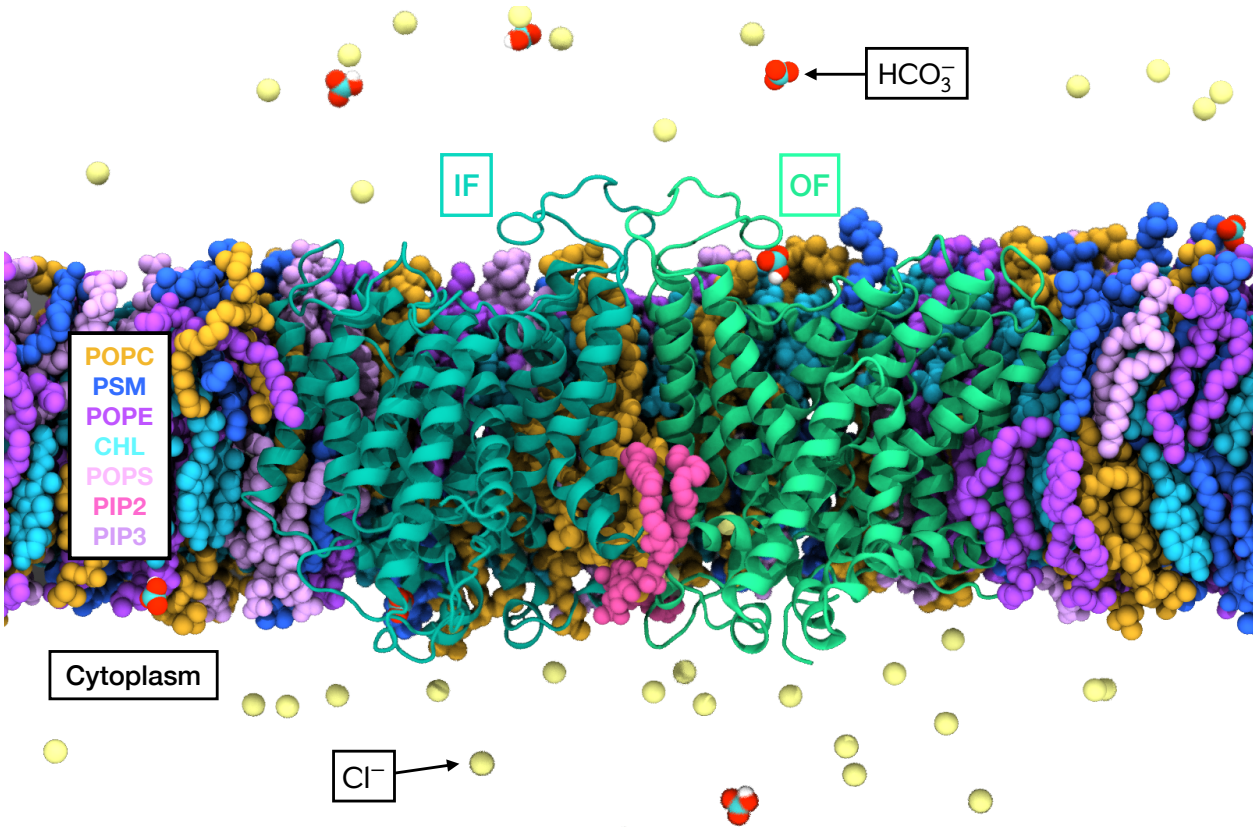

Figure 7: **Simulation system of membrane-embedded AE1 dimer.** The AE1 dimer embedded in a heterogeneous membrane. Multiple lipid types included in the bilayer are represented in distinct colors as labeled. Two AE1 protomers in the OF and IF1 states are in light and dark green cartoon representations respectively. The system is ionized with Cl^- and HCO_3^- shown as spheres, and neutralized with sodium ions (not shown). The interfacial PIP2 lipid is highlighted in pink.

tions.[73,74] Bonds involving hydrogen atoms were fixed using SHAKE and SETTLE algorithms.[75] A 2-fs timestep was utilized for both equilibrium simulations and production runs, unless specified otherwise.

After system preparation, we initiated a five-phase equilibration. During the initial phase, harmonic restraints of 10 kcal/mol/Å^2 were applied to protein backbone heavy atoms, and 5 kcal/mol/Å^2 to protein side chain and lipid head-group heavy atoms. This stage included 10,000 steps of conjugate gradient energy minimization followed by a 100 ps MD simulation with 0.5-fs timestep. For the subsequent three phases, each conducted for 500 ps, we employed a 1-fs timestep with sequentially halving the restraints on the proteins and lipids. In the final stages, the systems were equilibrated for 1 ns with a 2-fs timestep. Upon completing the equilibration stages, the production runs were performed for eight replicas, each spanning 1 µs, with all restraints removed.

Characterization of anion binding

Anions were considered interacting with AE1 when they were within 3.5 Å of any heavy atom of the protein. Anion density maps were generated by analyzing the averaged presence of anions in all simulations using the volumetric map tool in VMD. The ranking of the luminal anion-interacting residues was based on their frequency of anion binding in either state, determined by counting the number of frames in which anions bound to specific residues within the lumen throughout the simulations. The dissociation constant was calculated using the ratio of time the substrate was bound to

the residues relative to the total simulation time, representing the equilibrium between the bound and unbound states.

Biasing protocols with collective variables

The conformational transition from OF to IF state was induced using driven simulations. In this approach, biases are strategically applied to select atoms, promoting specific structural alterations of the system. We employed two system-specific collective variables (CVs) through the CV module in NAMD.[66,67] CVs describe various geometric relationships ranging from the basic ones, such as center of mass (COM) distances between atom groups, to more complex ones, such as radius of gyration or relative orientations among the protein's structural elements. The selection of the CVs was driven by empirical considerations and a comparative analysis of the OF and IF structures. The translational and rotational motions of the TD relative to the SD can nearly completely describe the conformational transition of AE1 between the two states. These motions can be best quantified by CVs z and θ,[76] as described in Fig. 4A. z is the distance between the COM of the TD and the SD (Cα atoms of TM helices only), and θ is the angle of the first principle axis of the TM helices of TD with respect to that in the IF structure when aligned with SD. Three systems were set up: *apo*, HCO_3^--bound, and HCO_3^--bound with cryo-EM PIP_2 lipids removed. The biasing restrains and pulling protocols were the same for all three systems. In the HCO_3^--bound system, an extra bond was introduced to effectively anchor the HCO_3^- to a pivotal binding residue, R730. This was done by a harmonic restraint between the carbon atom of HCO_3^- and R730 side chain, preventing substrate unbinding into solution during the transition. For each system, we first performed a 500 ns equilibrium simulation. Then driven simulation were done for 200 ns, followed by a 100-ns releasing stage in which the force constants of two CVs were gradually reduced. The final structures were then equilibrated for another 500 ns with no biases to ensure their stability.

String method with swarms of trajectories (SMwST)

The transition pathway derived from the driven simulations are inherently biased by the designated CV protocol used, indicating the need for subsequent relaxation to capture more energetically favorable transitions. SMwST functions as a path-finding and refinement algorithm optimized for multidimensional CVs.[41,77,78] It employs a multi-walker system, where each walker iteratively samples and fine-tunes the initial transition pathway. The process is iterated until convergence, represented by the stabilization of a local minimum energy pathway within the defined CV space. Within SMwST, the initial transition pathway is segmented into N equidistant points termed as "images". The positions of these images are refined by averaging over the net drift across M identical simulation replicas performed on them, named as the "swarms". The entire transition pathway was divided into 32 images (or windows) and 24 runs were launched from each image to sample regions near the trajectory in the CV space. Every cycle encompassed two stages: a 10-ps restrained simulation that anchored the M replicas to the current center, followed by a 10-ps unrestrained MD to allow for drift. These two-stage cycles facilitated drifting along the local free energy gradient. After each cycle, updates are made to the image centers, complemented by a smoothing and reparametrization procedure. For our AE1 system, we continued the SMwST runs for a total of 200 cycles, although convergence was achieved after around 100 iterations in all systems.

Bias-exchange umbrella sampling (BEUS)

To determine the free energy profile, or potential of mean force (PMF), along the optimized pathway, we employed 1D-BEUS calculations.[40,42] The refined trajectory obtained from SMwST was segmented into 64 windows (replicas). Each window was then simulated with a simulation in which a bias to its current center is employed, using a harmonic restraint with a force constant of 36 kcal/mol/Å^2. During the simulation, replica exchange is attempted every 1 ns,

allowing for the swapping of restraining centers between replicas in adjacent windows based on a Monte Carlo algorithm, thereby enhancing sampling efficiency. Each replica was sampled for 20 ns, resulting in a cumulative simulation time of 1.28 µs across all replicas. The convergence of the simulations and sufficient overlap between adjacent windows were confirmed by examining the histograms along each CV (Supplementary Fig. S6D and E). The sampled data are reweighted using the Weighted Histogram Analysis Method (WHAM) algorithm to generate free energy profiles along the refined pathways.[79]

Author Contribution

T.C. and E.T. designed, performed, and analyzed the MD simulations. F.V. and O.C. designed and performed the cryo-EM experiments for structure determination and analysis. K.K. assisted with cryo-EM data processing and figure preparation. E.G. and M.Q. designed and performed the uptake assay experiments. T.C. and E.T. wrote the manuscript with input from all authors.

References

[1] Rao, A. Disposition of the band 3 polypeptide in the human erythrocyte membrane. The reactive sulfhydryl groups. *Journal of Biological Chemistry* **1979**, *254*, 3503–3511.

[2] Reithmeier, R. A.; Casey, J. R.; Kalli, A. C.; Sansom, M. S.; Alguel, Y.; Iwata, S. Band 3, the human red cell chloride/bicarbonate anion exchanger (AE1, SLC4A1), in a structural context. *Biochimica et biophysica acta (BBA)-Biomembranes* **2016**, *1858*, 1507–1532.

[3] Doyle, J.; Cooper, J. S. Physiology, Carbon Dioxide Transport. **2018**,

[4] Westen, E. A.; Prange, H. D. A reexamination of the mechanisms underlying the arteriovenous chloride shift. *Physiological and Biochemical Zoology* **2003**, *76*, 603–614.

[5] Hamasaki, N. The role of band 3 protein in oxygen delivery by red blood cells. *Indian Journal of Clinical Biochemistry* **1999**, *14*, 49–58.

[6] Kay, M. Band 3 and its alterations in health and disease. *Cellular and molecular biology* **2004**, *50*, 117–138.

[7] Bruce, L. J.; Tanner, M. J. Erythroid band 3 variants and disease. *Best Practice & Research Clinical Haematology* **1999**, *12*, 637–654.

[8] Yenchitsomanus, P.-t.; Kittanakom, S.; Rungroj, N.; Cordat, E.; Reithmeier, R. A. Molecular mechanisms of autosomal dominant and recessive distal renal tubular acidosis caused by SLC4A1 (AE1) mutations. *Journal of molecular and genetic medicine: an international journal of biomedical research* **2005**, *1*, 49.

[9] Reinstein, E.; Scheffner, M.; Oren, M.; Ciechanover, A.; Schwartz, A. Degradation of the E7 human papillomavirus oncoprotein by the ubiquitin-proteasome system: targeting via ubiquitination of the N-terminal residue. *Oncogene* **2000**, *19*, 5944–5950.

[10] Vallese, F.; Kim, K.; Yen, L. Y.; Johnston, J. D.; Noble, A. J.; Calì, T.; Clarke, O. B. Architecture of the human erythrocyte ankyrin-1 complex. *Nature structural & molecular biology* **2022**, *29*, 706–718.

[11] Chu, H.; Low, P. S. Mapping of glycolytic enzyme-binding sites on human erythrocyte band 3. *Biochemical Journal* **2006**, *400*, 143–151.

[12] Barman, S.; Nayak, D. P. Analysis of the transmembrane domain of influenza virus neuraminidase, a type II transmembrane glycoprotein, for apical sorting and raft association. *Journal of virology* **2000**, *74*, 6538–6545.

[13] Shnitsar, V.; Li, J.; Li, X.; Calmettes, C.; Basu, A.; Casey, J. R.; Moraes, T. F.; Reithmeier, R. A. A substrate access tunnel in the cytosolic domain is not an essential feature of the solute carrier 4 (SLC4) family of bicarbonate transporters. *Journal of Biological Chemistry* **2013**, *288*, 33848–33860.

[14] Huynh, K. W.; Jiang, J.; Abuladze, N.; Tsirulnikov, K.; Kao, L.; Shao, X.; Newman, D.; Azimov, R.; Pushkin, A.; Zhou, Z. H.; Kurtz, I. CryoEM structure of the human SLC4A4 sodium-coupled acid-base transporter NBCe1. *Nature communications* **2018**, *9*, 900.

[15] Thurtle-Schmidt, B. H.; Stroud, R. M. Structure of Bor1 supports an elevator transport mechanism for SLC4 anion exchangers. *Proceedings of the National Academy of Sciences, USA* **2016**, *113*, 10542–10546.

[16] Zhekova, H. R.; Jiang, J.; Wang, W.; Tsirulnikov, K.; Kayık, G.; Khan, H. M.; Azimov, R.; Abuladze, N.; Kao, L.; Newman, D., et al. CryoEM structures of anion exchanger 1 capture multiple states of inward-and outward-facing conformations. *Communications Biology* **2022**, *5*, 1372.

[17] Capper, M. J.; Yang, S.; Stone, A. C.; Vatansever, S.; Zilberg, G.; Mathiharan, Y. K.; Habib, R.; Hutchinson, K.; Zhao, Y.; Schlessinger, A., et al. Substrate binding and inhibition of the anion exchanger 1 transporter. *Nature Structural & Molecular Biology* **2023**, *30*, 1495–1504.

[18] Arakawa, T. et al. Crystal structure of the anion exchanger domain of human erythrocyte band 3. *Science* **2015**, *350*, 680–684.

[19] Xia, X.; Liu, S.; Zhou, Z. H. Structure, dynamics and assembly of the ankyrin complex on human red blood cell membrane. *Nature structural & molecular biology* **2022**, *29*, 698–705.

[20] Pal, A.; Mehn, D.; Molnar, E.; Gedey, S.; Meszaros, P.; Nagy, T.; Glavinas, H.; Janaky, T.; von Richter, O.; Bathori, G., et al. Cholesterol potentiates ABCG2 activity in a heterologous expression system: improved in vitro model to study function of human ABCG2. *Journal of Pharmacology and Experimental Therapeutics* **2007**, *321*, 1085–1094.

[21] Aharonovitz, O.; Zaun, H. C.; Balla, T.; York, J. D.; Orlowski, J.; Grinstein, S. Intracellular pH regulation by Na+/H+ exchange requires phosphatidylinositol 4, 5-bisphosphate. *The Journal of cell biology* **2000**, *150*, 213–224.

[22] Zhang, W.; Ding, D.; Lu, Y.; Chen, H.; Jiang, P.; Zuo, P.; Wang, G.; Luo, J.; Yin, Y.; Luo, J.; Yin, Y. Structural and functional insights into the lipid regulation of human anion exchanger 2. *Nature Communications* **2024**, *15*, 759.

[23] Zhekova, H. R.; Echemendía, D. P. R.; Sejdiu, B. I.; Pushkin, A.; Tieleman, D. P.; Kurtz, I. Molecular dynamics simulations of lipid-protein interactions in SLC4 proteins. *Biophysical Journal* **2024**,

[24] Ficici, E.; Faraldo-Gómez, J. D.; Jennings, M. L.; Forrest, L. R. Asymmetry of inverted-topology repeats in the AE1 anion exchanger suggests an elevator-like mechanism. *Journal of General Physiology* **2017**, *149*, 1149–1164.

[25] Dutzler, R.; Campbell, E. B.; Cadene, M.; Chait, B. T.; MacKinnon, R. X-ray structure of a CLC chloride channel at 3.0 Å reveals the molecular basis of anion selectivity. *Nature* **2002**, *415*, 287–294.

[26] Wang, W.; Tsirulnikov, K.; Zhekova, H. R.; Kayık, G.; Khan, H. M.; Azimov, R.; Abuladze, N.; Kao, L.; Newman, D.; Noskov, S. Y., et al. Cryo-EM structure of the sodium-driven chloride/bicarbonate exchanger NDCBE. *Nature communications* **2021**, *12*, 5690.

[27] Pyle, E.; Kalli, A. C.; Amillis, S.; Hall, Z.; Lau, A. M.; Hanyaloglu, A. C.; Diallinas, G.; Byrne, B.; Politis, A. Structural lipids enable the formation of functional oligomers of the eukaryotic purine symporter UapA. *Cell chemical biology* **2018**, *25*, 840–848.

[28] Mandala, V. S.; McKay, M. J.; Shcherbakov, A. A.; Dregni, A. J.; Kolocouris, A.; Hong, M. Structure and drug binding of the SARS-CoV-2 envelope protein transmembrane domain in lipid bilayers. *Nature Structural & Molecular Biology* **2020**, *27*, 1202–1208.

[29] Sritippayawan, S.; Sumboonnanonda, A.; Vasuvattakul, S.; Keskanokwong, T.; Sawasdee, N.; Paemanee, A.; Thuwajit, P.; Wilairat, P.; Nimmannit, S.; Malasit, P., et al. Novel compound heterozygous SLC4A1 mutations in Thai patients with autosomal recessive distal renal tubular acidosis. *American journal of kidney diseases* **2004**, *44*, 64–70.

[30] Dalmark, M.; Wieth, J. O. Temperature dependence of chloride, bromide, iodide, thiocyanate and salicylate transport in human red cells. *The Journal of Physiology* **1972**, *224*, 583–610.

[31] Salhany, J. M.; Schopfer, L. M. Kinetic mechanism of DIDS binding to band 3 (AE1) in human erythrocyte membranes. *Blood Cells, Molecules, and Diseases* **2001**, *27*, 844–849.

[32] Drew, D.; North, R. A.; Nagarathinam, K.; Tanabe, M. Structures and general transport mechanisms by the major facilitator superfamily (MFS). *Chemical reviews* **2021**, *121*, 5289–5335.

[33] Herrington, W.; Nye, H.; Hammersley, M.; Watkinson, P. Are arterial and venous samples clinically equivalent for the estimation of pH, serum bicarbonate and potassium concentration in critically ill patients? *Diabetic medicine* **2012**, *29*, 32–35.

[34] Galanter, W. L.; Labotka, R. J. The binding of nitrate to the human anion exchange protein (AE1) studied with 14N nuclear magnetic resonance. *Biochimica et Biophysica Acta (BBA)-Protein Structure and Molecular Enzymology* **1991**, *1079*, 146–151.

[35] Mitchell, P. A general theory of membrane transport from studies of bacteria. *Nature* **1957**, *180*, 134–136.

[36] Jardetzky, O. Simple allosteric model for membrane pumps. *Nature* **1966**, *211*, 969–970.

[37] Fiorin, G.; Klein, M. L.; Hénin, J. Using Collective Variables to Drive Molecular Dynamics Simulations. *Molecular Physics* **2013**, *111*, 3345–3362.

[38] Chen, I.; Pant, S.; Wu, Q.; Cater, R.; Sobti, M.; Vandenberg, R.; Stewart, A. G.; Tajkhorshid, E.; Font, J.; Ryan, R. Glutamate transporters have a chloride channel with two hydrophobic gates. *Nature* **2021**, *591*, 327–331.

[39] Pant, S.; Wu, Q.; Ryan, R.; Tajkhorshid, E. Microscopic Characterization of the Chloride Permeation Pathway in the Human Excitatory Amino Acid Transporter 1 (EAAT1). *ACS Chemical Neuroscience* **2022**, *13*, 776–785.

[40] Moradi, M.; Tajkhorshid, E. Mechanistic picture for conformational transition of a membrane transporter at atomic resolution. *Proceedings of the National Academy of Sciences, USA* **2013**, *110*, 18916–18921.

[41] Pan, A. C.; Sezer, D.; Roux, B. Finding transition pathways using the string method with swarms of trajectories. *Journal of Physical Chemistry B* **2008**, *112*, 3432–3440.

[42] Moradi, M.; Tajkhorshid, E. Computational recipe for efficient description of large-scale conformational changes in biomolecular systems. *Journal of Chemical Theory and Computation* **2014**, *10*, 2866–2880.

[43] Infield, D. T.; Rasouli, A.; Galles, G. D.; Chipot, C.; Tajkhorshid, E.; Ahern, C. A. Cation-π interactions and their functional roles in membrane proteins. *Journal of molecular biology* **2021**, *433*, 167035.

[44] Kumar, K.; Woo, S. M.; Siu, T.; Cortopassi, W. A.; Duarte, F.; Paton, R. S. Cation–π interactions in protein–ligand binding: Theory and data-mining reveal different roles for lysine and arginine. *Chemical science* **2018**, *9*, 2655–2665.

[45] Armstrong, C. T.; Mason, P. E.; Anderson, J. R.; Dempsey, C. E. Arginine side chain interactions and the role of arginine as a gating charge carrier in voltage sensitive ion channels. *Scientific reports* **2016**, *6*, 21759.

[46] Hsiao, C.-T.; Wang, P.-W.; Chang, H.-C.; Chen, Y.-Y.; Wang, S.-H.; Chern, Y.; Khoo, K.-H. Advancing a high throughput glycotope-centric glycomics workflow based on nanoLC-MS2-product dependent-MS3 analysis of permethylated glycans. *Molecular & Cellular Proteomics* **2017**, *16*, 2268–2280.

[47] Lu, Y.; Zuo, P.; Chen, H.; Shan, H.; Wang, W.; Dai, Z.; Xu, H.; Chen, Y.; Liang, L.; Ding, D., et al. Structural insights into the conformational changes of BTR1/SLC4A11 in complex with PIP2. *Nature Communications* **2023**, *14*, 6157.

[48] Niggli, V.; Carafoli, E. The Plasma Membrane Ca 2+ ATPase: Purification by Calmodulin Affinity Chromatography, and Reconstitution of the Purified Protein. *P-Type ATPases: Methods and Protocols* **2016**, 57–70.

[49] Suloway, C.; Shi, J.; Cheng, A.; Pulokas, J.; Carragher, B.; Potter, C. S.; Zheng, S. Q.; Agard, D. A.; Jensen, G. J. Fully automated, sequential tilt-series acquisition with Leginon. *Journal of structural biology* **2009**, *167*, 11–18.

[50] Punjani, A.; Rubinstein, J. L.; Fleet, D. J.; Brubaker, M. A. cryoSPARC: algorithms for rapid unsupervised cryo-EM structure determination. *Nature methods* **2017**, *14*, 290–296.

[51] Wagner, T.; Merino, F.; Stabrin, M.; Moriya, T.; Antoni, C.; Apelbaum, A.; Hagel, P.; Sitsel, O.; Raisch, T.; Prumbaum, D., et al. SPHIRE-crYOLO is a fast and accurate fully automated particle picker for cryo-EM. *Communications biology* **2019**, *2*, 218.

[52] Zivanov, J.; Nakane, T.; Scheres, S. H. A Bayesian approach to beam-induced motion correction in cryo-EM single-particle analysis. *IUCrJ* **2019**, *6*, 5–17.

[53] Emsley, P.; Lohkamp, B.; Scott, W. G.; Cowtan, K. Features and development of Coot. *Acta Crystallographica D* **2010**, *66*, 486–501.

[54] Casañal, A.; Lohkamp, B.; Emsley, P. Current developments in Coot for macromolecular model building of Electron Cryo-microscopy and Crystallographic Data. *Protein Science* **2020**, *29*, 1055–1064.

[55] Meng, E. C.; Goddard, T. D.; Pettersen, E. F.; Couch, G. S.; Pearson, Z. J.; Morris, J. H.; Ferrin, T. E. UCSF ChimeraX: Tools for structure building and analysis. *Protein Science* **2023**, *32*, e4792.

[56] Hagenah, L. M.; Dhingra, S. K.; Small-Saunders, J. L.; Qahash, T.; Willems, A.; Schindler, K. A.; Rangel, G. W.; Gil-Iturbe, E.; Kim, J.; Akhundova, E., et al. Additional PfCRT mutations driven by selective pressure for improved fitness can result in the loss of piperaquine resistance and altered Plasmodium falciparum physiology. *Mbio* **2024**, *15*, e01832–23.

[57] Kim, D. E.; Chivian, D.; Baker, D. Protein structure prediction and analysis using the Robetta server. *Nucleic acids research* **2004**, *32*, W526–W531.

[58] Søndergaard, C. R.; Olsson, M. H.; Rostkowski, M.; Jensen, J. H. Improved treatment of ligands and coupling effects in empirical calculation and rationalization of pKa values. *Journal of Chemical Theory and Computation* **2011**, *7*, 2284–2295.

[59] Humphrey, W.; Dalke, A.; Schulten, K. VMD: visual molecular dynamics. *Journal of Molecular Graphics* **1996**, *14*, 33–38.

[60] Wu, E.; Cheng, X.; Jo, S.; Rui, H.; Song, K.; Dávila-Contreras, E.; Qi, Y.; Lee, J.; Monje-Galvan, V.; Venable, R.; Klauda, J.; Im, W. CHARMM-GUI Membrane Builder Toward Realistic Biological Membrane Simulations. *Journal of Computational Chemistry* **2014**, *35*, 1997–2004.

[61] Jo, S.; Lim, J. B.; Klauda, J. B.; Im, W. CHARMM-GUI Membrane Builder for Mixed Bilayers and its Application to Yeast Membranes. *Biophysical Journal* **2009**, *97*, 50–58.

[62] Melzak, K. A.; Muth, M.; Kirschhöfer, F.; Brenner-Weiss, G.; Bieback, K. Lipid ratios as a marker for red blood cell storage quality and as a possible explanation for donor gender differences in storage quality. *Vox sanguinis* **2020**, *115*, 655–663.

[63] Dodge, J. T.; Phillips, G. B. Composition of phospholipids and of phospholipid fatty acids and aldehydes in human red cells. *Journal of Lipid Research* **1967**, *8*, 667–675.

[64] Lomize, M. A.; Pogozheva, I. D.; Joo, H.; Mosberg, H. I.; Lomize, A. L. OPM database and PPM web server: resources for positioning of proteins in membranes. *Nucleic Acids Research* **2012**, *40*, D370–376.

[65] Licari, G.; Dehghani-Ghahnaviyeh, S.; Tajkhorshid, E. Membrane Mixer: A Toolkit for Efficient Shuffling of Lipids in Heterogeneous Biological Membranes. *Journal of Chemical Information and Modeling* **2022**, *62*, 986–996.

[66] Phillips, J. C.; Braun, R.; Wang, W.; Gumbart, J.; Tajkhorshid, E.; Villa, E.; Chipot, C.; Skeel, R. D.; Kale, L.; Schulten, K. Scalable molecular dynamics with NAMD. *Journal of Computational Chemistry* **2005**, *26*, 1781–1802.

[67] Phillips, J. C. et al. Scalable molecular dynamics on CPU and GPU architectures with NAMD. *Journal of Chemical Physics* **2020**, *153*, 044130.

[68] Huang, J.; Rauscher, S.; Nawrocki, G.; Ran, T.; Feig, M.; de Groot, B. L.; Grubmüller, H.; MacKerell Jr, A. D. CHARMM36m: an improved force field for folded and intrinsically disordered proteins. *Nature Methods* **2017**, *14*, 71–73.

[69] Klauda, J. B.; Venable, R. M.; Freites, J. A.; O'Connor, J. W.; Tobias, D. J.; Mondragon-Ramirez, C.; Vorobyov, I.; MacKerell Jr., A. D.; Pastor, R. W. Update of the CHARMM all-atom additive force field for lipids: Validation on six lipid types. *Journal of Physical Chemistry B* **2010**, *114*, 7830–7843.

[70] Hoover, W. G. Canonical Dynamics: Equilibrium Phase-Space Distributions. *Physical Review A* **1985**, *31*, 1695–1697.

[71] Martyna, G. J.; Tobias, D. J.; Klein, M. L. Constant pressure molecular dynamics algorithms. *Journal of Chemical Physics* **1994**, *101*, 4177–4189.

[72] Feller, S. E.; Zhang, Y.; Pastor, R. W. Constant pressure molecular dynamics simulation: the Langevin piston method. *Journal of Chemical Physics* **1995**, *103*, 4613–4621.

[73] Darden, T.; York, D.; Pedersen, L. Particle mesh Ewald: an $N{\cdot}\log(N)$ method for Ewald sums in large systems. *Journal of Chemical Physics* **1993**, *98*, 10089–10092.

[74] Essmann, U.; Perera, L.; Berkowitz, M. L.; Darden, T.; Lee, H.; Pedersen, L. G. A smooth particle mesh Ewald method. *Journal of Chemical Physics* **1995**, *103*, 8577–8593.

[75] Miyamoto, S.; Kollman, P. A. Settle: an analytical version of the SHAKE and RATTLE algorithm for rigid water molecules. *Journal of Computational Chemistry* **1992**, *13*, 952–962.

[76] Sauer, D. B.; Trebesch, N.; Marden, J. J.; Cocco, N.; Song, J.; Koide, A.; Koide, S.; Tajkhorshid, E.; Wang, D.-N. Structural basis for the reaction cycle of DASS dicarboxylate transporters. *eLife* **2020**, *9*, e61350.

[77] Jiang, W.; Phillips, J. C.; Huang, L.; Fajer, M.; Meng, Y.; Gumbart, J. C.; Luo, Y.; Schulten, K.; Roux, B. Generalized Scalable Multiple Copy Algorithms for Molecular Dynamics Simulations in NAMD. *Computer Physics Communications* **2014**, *185*, 908–916.

[78] Moradi, M.; Enkavi, G.; Tajkhorshid, E. Atomic-level characterization of transport cycle thermodynamics in the glycerol-3-phosphate:phosphate transporter. *Nature Communications* **2015**, *6*, 8393.

[79] Souaille, M.; Roux, B. Extension to the weighted histogram analysis method: combining umbrella sampling with free energy calculations. *Computer Physics Communications* **2001**, *135*, 40–57.